Published in "Swiss Journal of Geosciences 111(3): 383–398, 2018"
which should be cited to refer to this work.

Multi-proxy facies analysis of the Opalinus Clay and depositional implications (Mont Terri rock laboratory, Switzerland)

Bruno Lauper[1] · David Jaeggi[2] · Gaudenz Deplazes[3] · Anneleen Foubert[1]

Abstract
Located in NW Switzerland, the Mont Terri rock laboratory is a research facility primarily investigating the Opalinus Clay as potential host rock for deep geological disposal of radioactive waste. In the Mont Terri area, this Jurassic shale formation is characterized by three distinctive lithofacies: a shaly facies, a carbonate-rich sandy facies and a sandy facies. However, the lithological variability at dm- to cm-scale is not yet fully understood and a detailed lithofacies characterization is currently lacking. Within the present study, petrographic descriptions at micro- and macro-scale, geophysical core logging (P-wave velocity and gamma-ray density), geochemical core logging (X-ray fluorescence) and organic matter quantification (Rock-Eval pyrolysis) were combined on a 27.6 m long Opalinus Clay drillcore comprising the three major lithofacies. The high-resolution investigation of the core resulted into a refinement of the three-fold lithofacies classification, and revealed high intra-facies heterogeneity. Five subfacies were defined and linked to distinctive depositional regimes. The studied succession is interpreted as a shallowing-upward trend within a storm-wave-dominated epicontinental sea characterized by relative shallow water depths.

Keywords Mudstones · Early-Middle Jurassic · Sedimentary petrography · Multi-sensor core logger · XRF core scanner · Rock-Eval pyrolysis

1 Introduction

The Opalinus Clay, a shale formation of late Toarcian to early Aalenian in age, was selected by Nagra (National Cooperative for the Disposal of Radioactive Waste) as future host rock for the deep geological disposal of radioactive waste in Switzerland. Several partner organizations considering shale formations as potential repository host rocks initiated an international research program on the Opalinus Clay (the Mont Terri Project) and addressed numerous properties of this formation in the dedicated Mont Terri rock laboratory (e.g. Thury and Bosart 1999; Bossart and Thury 2008; Bossart et al. 2017).

Previous petrographic studies in the Mont Terri area showed that the Opalinus Clay is composed of five subunits characterized by three distinctive lithofacies (Bläsi et al. 1991; Hostettler et al. 2017). Further to the east, the Opalinus Clay shows different lithofacies successions (e.g. Bläsi 1987; Matter et al. 1987, 1988; Wetzel and Allia 2000, 2003; Nagra 2001). This W–E lateral variability suggests that sediment deposition in the Mont Terri area may have been influenced by different factors (e.g. Hostettler et al. 2017). Nonetheless, a depositional model has not been established yet for this area.

The present research investigates in more detail the dm- to cm-scale heterogeneity of the Opalinus Clay in the Mont Terri rock laboratory, and discusses some implications for the depositional setting, particularly in the frame of the so-called SO-Experiment (Sedimentology of Opalinus Clay; see also Müller and Jaeggi 2012). Furthermore, there is increasing interest to develop (semi-)quantitative methods for characterization of small-scale lithological variability at

✉ Bruno Lauper
bruno.lauper@unifr.ch

[1] Department of Geosciences, University of Fribourg, Chemin du Musée 6, 1700 Fribourg, Switzerland

[2] Federal Office of Topography swisstopo, Seftigenstrasse 264, 3084 Wabern, Switzerland

[3] National Cooperative for the Disposal of Radioactive Waste (Nagra), Hardstrasse 73, 5430 Wettingen, Switzerland

high-resolution. The present multi-proxy analytical study of the Opalinus Clay is the first step.

2 Geographical and geological setting

The Mont Terri rock laboratory is composed of 700 m of galleries and niches situated besides the security gallery of the Mont Terri motorway tunnel (Fig. 1). Located northwest of the town of St-Ursanne (Canton of Jura, Switzerland), the access to the rock laboratory is provided through the security gallery of the tunnel. The Mont Terri motorway tunnel crosses the northernmost anticline of the Jura Mountains, the Mont Terri anticline (Fig. 2). This anticline is located at a disruption of the Muschelkalk decollement, and its complex geometry is influenced by the Rhine–Bresse Graben transfer zone (Nussbaum et al. 2011; Caër et al. 2015).

In the Mont Terri area, the outcropping sedimentary rocks range from Middle Triassic to Quaternary. The late Palaeozoic clastic sediments are covered by 800 m of Mesozoic sandstones, limestones, dolomites, evaporites, marls and mudrocks, and locally by Cenozoic Molasse and Quaternary fluvio-glacial sediments (Nussbaum et al. 2011). Situated 300 m below the surface, the rock laboratory is entirely located within the 130 m thick Opalinus Clay (Hostettler et al. 2017). Previous studies estimated however an apparent thickness of about 150 m (Bläsi et al. 1991) to 160 m (Bossart and Thury 2008). The structurally complex frame of the Mont Terri anticline makes difficult to determine the true thickness of the formation. Further to the east, the formation shows an average thickness typically varying between 80 and 120 m (e.g. Bläsi 1987; Nagra 2002; Wetzel and Allia 2003). The Opalinus Clay rests on the Early Jurassic siltstone-marl-dominated Staffelegg Formation (Reisdorf et al. 2011). The overlying Passwang Formation consists of a series of parasequences characterized by mud, sandy marls, biodetritic limestones and iron oolites (Burkhalter 1996).

The Opalinus Clay represents an overconsolidated shale consisting of clay minerals (illite, illite–smectite mixed layers, kaolinite and chlorite), quartz grains (silt to fine sand fraction) and carbonates (bioclasts, cements, micrite and concretions), minor components are mica, feldspar, pyrite and organic matter (e.g. Nagra 2002; Bossart and Thury 2008; Mazurek 2011; Lerouge et al. 2014). Lithology varies regionally and the formation is typically subdivided into several lithofacies (e.g. Bläsi 1987; Matter et al. 1987, 1988; Nagra 2001, 2002; Wetzel and Allia 2003). In the Mont Terri area, five lithostratigraphic subunits are characterized by three lithofacies (Bläsi et al. 1991; Hostettler et al. 2017; Fig. 3): (lower) shaly facies; carbonate-rich sandy facies; (lower) sandy facies; (upper) shaly facies and (upper) sandy facies.

3 Materials and methods

A 27.6 m long drillcore (BDM-B2) penetrating the three major lithofacies is the base of this study. Starting in the MI-niche, the core was drilled perpendicular to the bedding (angle of dip = 43.8°) and with an azimuth of 150° (see

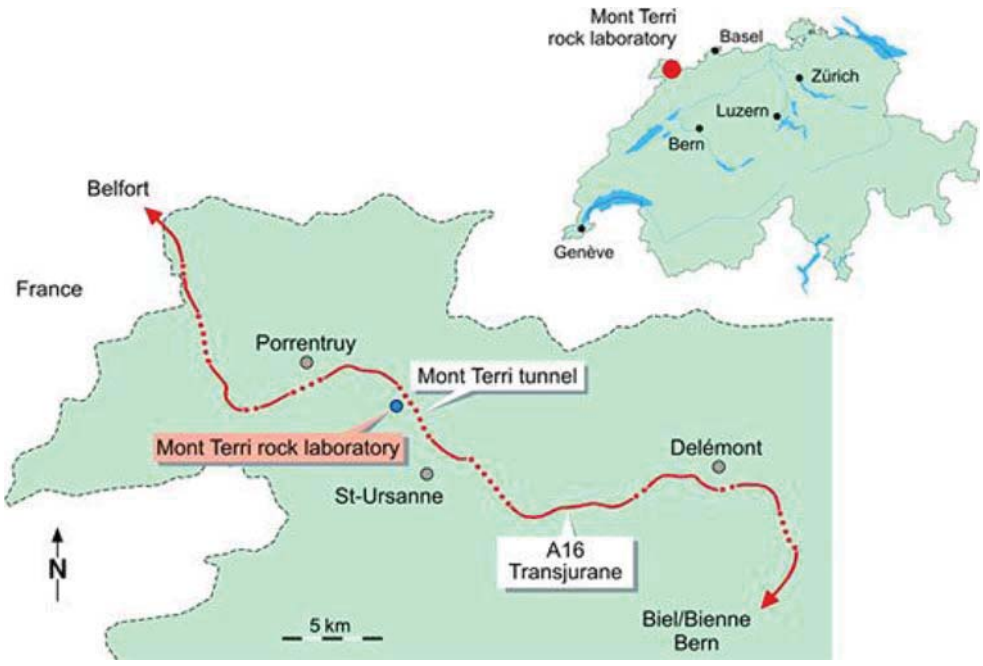

Fig. 1 Location map of the Mont Terri rock laboratory and outline of the A16 motorway. From Swisstopo, Mont Terri Project

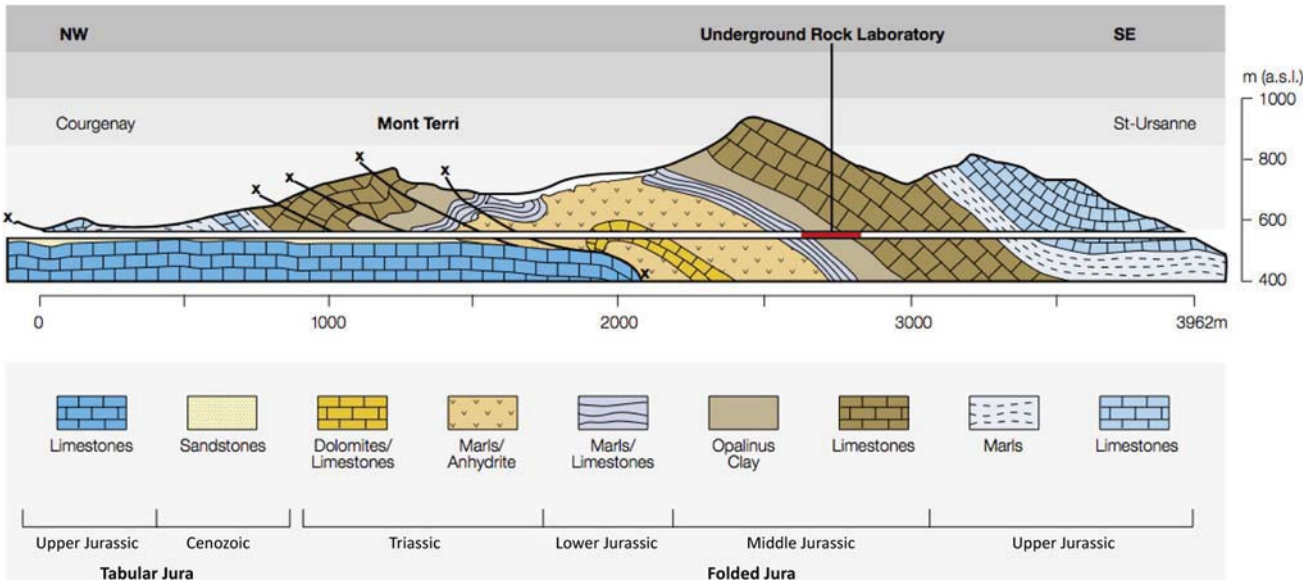

Fig. 2 Simplified geological profile along the Mont Terri motorway tunnel. The location of the Mont Terri rock laboratory is indicated in red. Positions of the main faults are indicated. Modified after Freivogel and Huggenberger (2003)

Fig. 3). Due to the low quality of the BDM-B2 core, it was embedded in transparent polyethylene tubes filled with an epoxy resin (Sika® Injection-26) before logging and analyses.

Detailed lithological descriptions were performed on the split core sections. The DMT CoreScan3 (DMT Group, Essen, Germany) available at the Mont Terri rock laboratory allowed the acquisition of optical images for improvement of sedimentary structures recognition. 24 thin sections were acquired at representative depths and studied with classical transmitted light petrographic microscopy (see Fig. 4 for location). Thin sections were stained with potassium ferricyanide and alkaline red S in acid solution for distinguishing carbonate minerals (Dickson 1965). Thin sections were used to examine microfacies variation, small-scale sedimentary structures, compositional and textural changes, and degree of bioturbation. The nomenclature scheme proposed by Lazar et al. (2015) was used for the description of composition and grain size. Bedding was described after Reineck and Wunderlich (1968), and degree of bioturbation was estimated using the bioturbation index (BI; from 1 to 5; see Lazar et al. 2015 and references therein).

Geophysical core logging was performed with a multi-sensor core logger (Geotek Limited, Daventry, UK) installed at the University of Bern (Switzerland). Gamma density and P-wave velocity were measured at a spatial resolution of 0.5 cm. For gamma density measurement, the gamma beam has been emitted at 662 keV through a 2.5 mm diameter collimator, using a 10 mCi ^{137}Cs capsule as gamma-ray source. Two rolling ARC transducers with a piezoelectric crystal as active element, surrounded by oil and encapsulated in soft epoxy, were used for P-wave velocity measurement. Pulse frequency was set at 230 kHz and timing resolution was 50 ns. The datasets were then calibrated and outliers removed.

Geochemical (X-ray diffraction) logging was performed with the ITRAX Core Scanner (Cox Analytical Systems, Mölndal, Sweden) installed at the University of Bern (Switzerland). It was equipped with a 3 kW Molybdenum X-ray tube. The X-ray voltage and current were set at 30 kV and 35 mA, respectively. The split core sections were analysed at a resolution of 1 cm and 10 s exposure time. A standard adjustment and refinement of the peak-fitting parameters using representative parts of the core sample was performed.

Total organic carbon (TOC) and mineral inorganic carbon (MinC) were identified by Rock-Eval pyrolysis method. In total, 120 samples of a few cubic centimetres of consolidated sediment were sampled about every 20 cm along the core. Each sample was grinded and homogenized into fine powder ($\sim$ 10 µm) in an agate mortar. The Turbo Rock-Eval 6 apparatus (Vinci Technologies, Nanterre, France) installed at the University of Lausanne (Switzerland) was used for the analysis.

Rock-Eval data allow the recognition of kerogen types by the use of a hydrogen index (HI) vs. oxygen index (OI) diagram (e.g. Espitalié et al. 1985). The HI is derived from the ratio of hydrogen to TOC and the OI refers to the ratio of CO_2 to TOC. Four kerogen types can be identified (Espitalié et al. 1985; McCarthy et al. 2011): type I kerogen reflects a lacustrine setting, type II kerogen reflects a marine setting, type III kerogen indicates a terrestrial origin and type IV kerogen is usually associated to reworked,

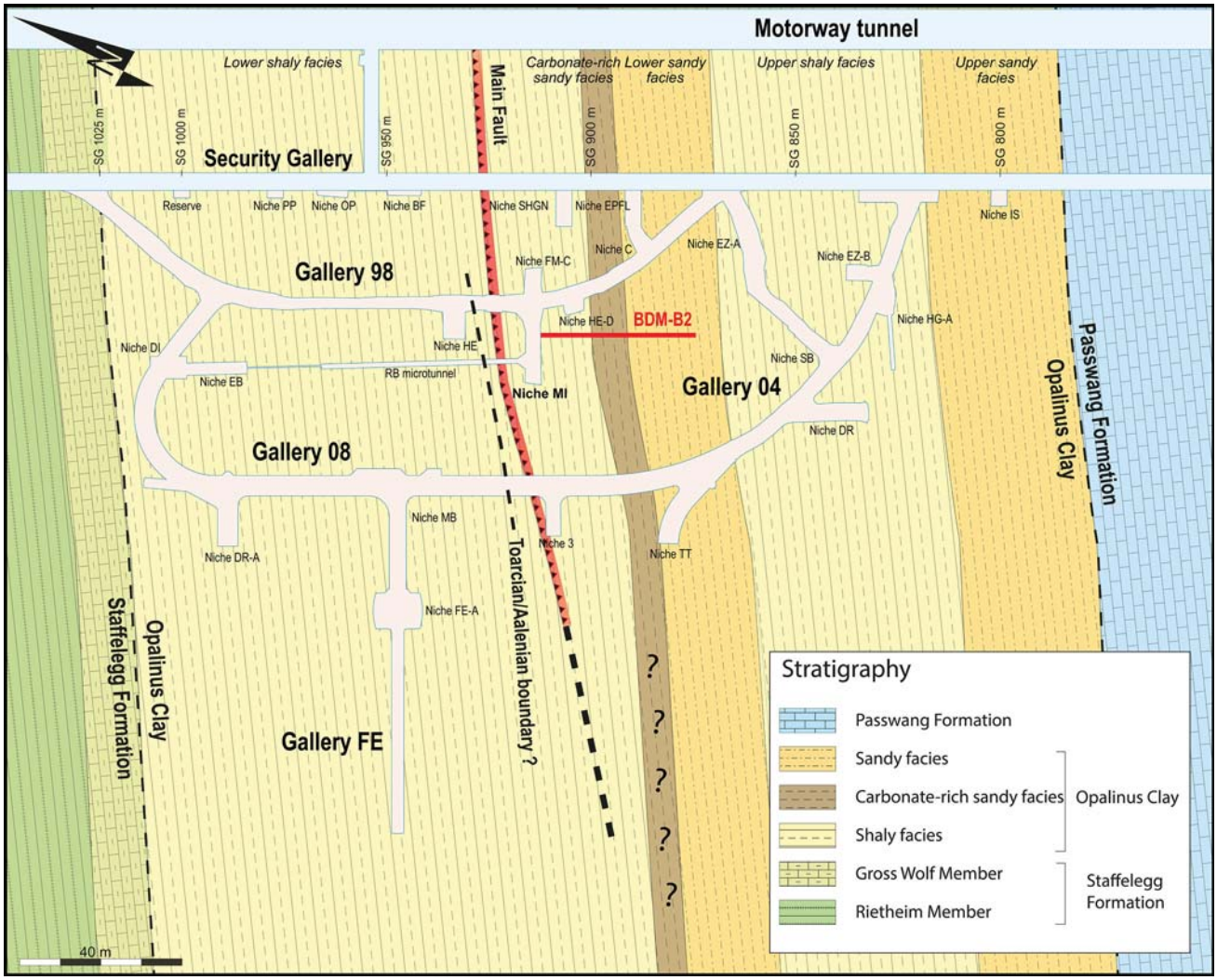

Fig. 3 Map of the Mont Terri rock laboratory with distribution and thicknesses of major lithofacies. Position of the BDM-B2 core is indicated in red. A major fault (Main Fault) is indicated within the lower shaly facies. The probable Toarcian/Aalenian boundary is represented by a dashed line (see Reisdorf et al. 2014). Modified after Swisstopo, Mont Terri Project

oxidized material. The S2 vs. TOC diagram provides an alternative method for kerogen type identification, where the S2 parameter refers to hydrocarbons generated by the Rock-Eval pyrolysis, measured in mg HC/g rock (Langford and Blanc-Valleron 1990). Such a graph allows to determine the regression equations of the Rock-Eval data, from which the HI can be inferred and associated to kerogen types. Type I kerogen can yield up to 80 wt% hydrocarbons during pyrolysis (HI = 800 mg/g TOC), type II kerogen can yield up to 50–60 wt% hydrocarbons (HI of 500–600) and type III kerogen yields at most 15–30 wt% hydrocarbons (HI of 150–300; Espitalié et al. 1985). The S2 vs. TOC diagram allows also to measuring the adsorption of hydrocarbon by the rock matrix. The so-called matrix effect is indicated by a positive x-intercept on the graph and corresponds to the threshold amount of organic material that must be present before enough hydrocarbons can be detected during pyrolysis (Langford and Blanc-Valleron 1990). Since clay is the main agent of adsorption, determining the matrix effect of a suite of samples gives an indication about the relative clay content (Espitalié et al. 1985).

4 Petrographic characterization

The macroscopic and microscopic petrographic study of the BDM-B2 core evidences the succession of three major lithofacies. The core consists of 7.28 m shaly facies, 6.76 m carbonate-rich sandy facies and 13.34 m sandy facies. Small-scale, intra-facies variation is identified and results into the definition of five subfacies (SF1–SF5; Fig. 4; Table 1).

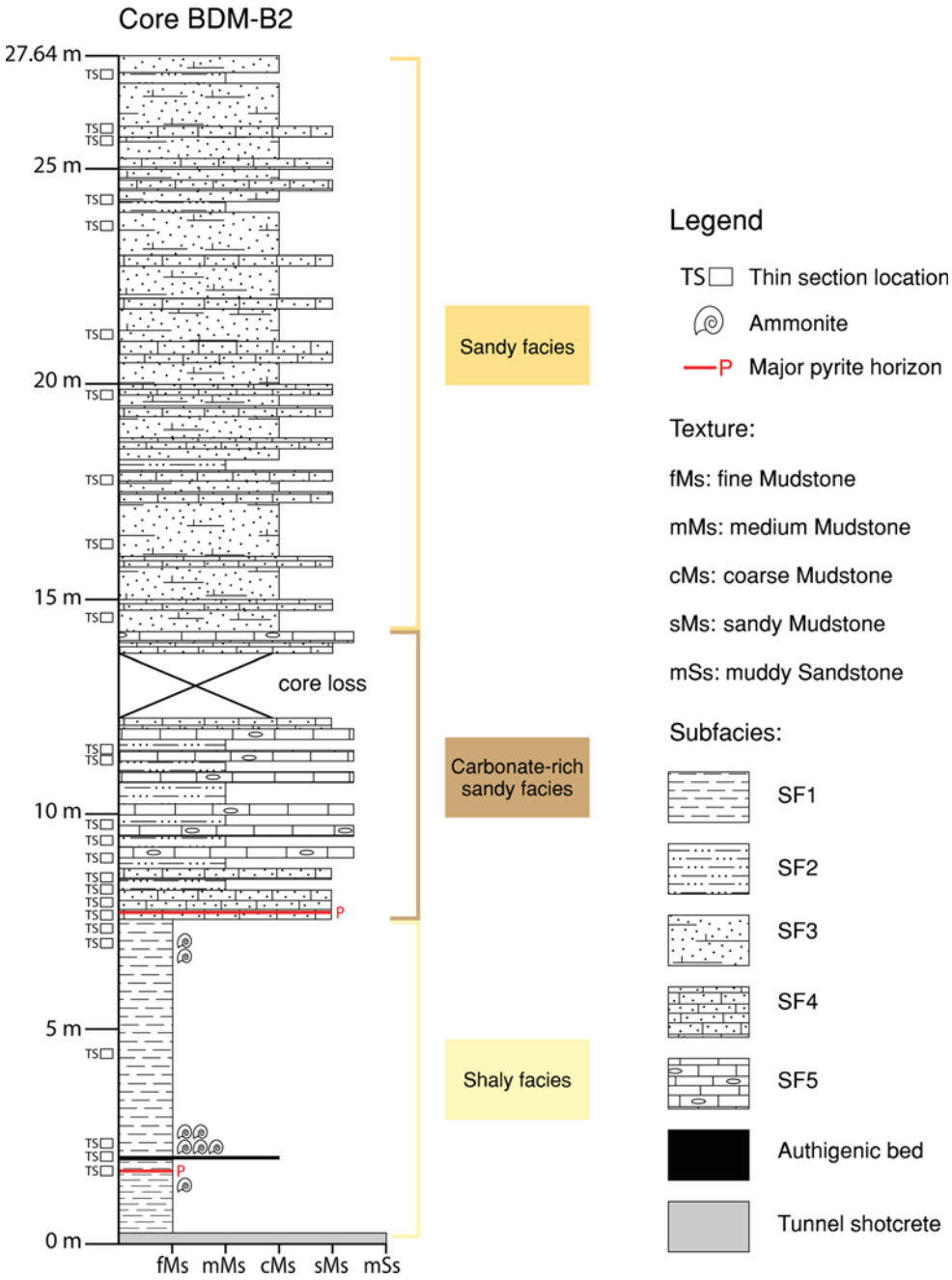

Fig. 4 Overview of the BDM-B2 core with lithofacies and subfacies distribution at dm-scale. Further subfacies variations occur at cm-scale, but could not be illustrated in this overview figure for scale purposes. The illustrated subfacies intervals correspond to lithological intervals dominated by the symbolized subfacies. Locations of thins sections (TS) are reported along the core

4.1 Definition of subfacies

Argillaceous subfacies (SF1) consists of dark grey, homogeneous, argillaceous mudstone (Figs. 5a, 6a). Grain size ranges between clay and very fine silt (< 8 μm). Some coarser, angular quartz grains (< 100 μm) occur throughout the matrix, or as round lenses (interpreted as burrows). Numerous mm long shell fragments (mainly *Bositra buchi* sp.) are present, typically enriched in certain horizons. Dispersed framboidal pyrite occurs throughout the matrix, while massive pyrite occurs in concretions and in cm thick horizons. Sparse cm thick carbonate nodules are observed. Typical composition comprises > 50% clay minerals, 10–30% quartz, < 10% carbonate and < 5% pyrite and other minor components.

Laminated subfacies (SF2) alternates argillaceous mud and siliceous/calcareous, sandy laminae (Figs. 5b, 6b). The argillaceous mud (< 8 μm) appears principally as matrix, or as thin laminae. It is mostly composed of clay minerals with some dispersed quartz grains (< 100 μm). The sandy laminae are continuous to discontinuous, occasionally graded and typically sharply delimitated. Some occur

Table 1 Sedimentary key attributes for distinguishing the five defined subfacies within the BDM-B2 core

Core BDM-B2	Sedimentary petrography				
	Colour	Grain size	Composition	Bioturbation	Structure/bedding
SF1	Dark grey	Fine mudstone	Argillaceous	Weakly bioturbated	Homogeneous
SF2	Medium-dark grey	Medium mudstone	Argillaceous–siliceous	Sparsely bioturbated	Laminated
SF3	Medium grey	Coarse to sandy mudstone	Siliceous–argillaceous	Moderately bioturbated	Lenticular
SF4	Medium-light grey	Sandy mudstone to muddy sandstone	Siliceous–calcareous	Strongly bioturbated	Lenticular to flaser
SF5	Light grey	Sandy mudstone to muddy sandstone	Calcareous	Churned	Homogeneous

rather as elongated lenses. They are composed of angular to subangular quartz silt to fine sand (32–150 μm) mixed with bioclastic fragments. They are cemented by sparitic Fe-rich calcite. Some laminae are almost pure quartz, while others are mostly bioclastics. Bioclasts are mainly echinoderm and shell fragments. They can reach up to 500 μm. Small starved ripples are commonly observed. Bioturbational structures are rare, although occasional round burrows occur (BI = 1–2). Typical composition comprises > 50% clay minerals, 10–25% quartz, 10–25% carbonate and < 5% pyrite and other minor components.

Lenticular subfacies (SF3) consists of lenticular-bedded, siliceous-argillaceous, sandy mudstone (Figs. 5c, 6c). It is composed of an argillaceous muddy matrix comprising numerous up to 1 cm long, thick lenses, typically composed of angular to subangular quartz coarse silt to fine sand (32–150 μm) and sparse to abundant bioclastic fragments (< 500 μm), cemented by sparitic Fe-rich calcite. A moderate degree of bioturbation (BI = 3) is assumed. Dispersed quartz grains and pyrite framboids occur throughout the muddy matrix. Some starved ripples and small ripple marks can be recognized between numerous bioturbational structures. Typical composition comprises 40–60% clay minerals, 20–40% quartz, 20–30% carbonates, < 5% pyrite and other minor components.

Sandy subfacies (SF4) consists of wavy- to flaser-bedded, siliceous-calcareous, sandy mudstone to muddy sandstone (Figs. 5d, 6d). The matrix is composed of mud, angular to subangular quartz grains (coarse silt to fine sand; 32–150 μm) and small bioclastic fragments (echinoderm, gastropod, bivalve, brachiopod; up to 2 mm) homogenized by bioturbation (Fig. 6e). Due to the high degree of bioturbation (BI = 4–5), the identification of primary sedimentary structures is challenging. A few ripple marks and mud drapes were however identified. Some sharply delimited, thick lenses and round burrows—sometimes pyritized—are still visible (Fig. 5e). Silt and sand grains are mostly cemented by sparitic Fe-rich calcite, while single mica flakes, framboidal pyrite and argillaceous floccules are dispersed within the matrix. Typical composition comprises 30–40% clay minerals, 40–50% quartz, 30–50% carbonates, < 5% pyrite and other minor components.

Bioclastic subfacies (SF5) consists of light grey, homogeneous, calcareous (or bioclastic), sandy mudstone to muddy sandstone (Figs. 5f, 6f). It shows numerous, up to several mm thick bioclasts and angular to subangular quartz grains (32–150 μm). The bioclasts are of high diversity with respect to size and origin (up to several mm; Fig. 6g). They are typically composed of fragments of echinoderms (crinoids, echinoids), bivalves, brachiopods and gastropods (Fig. 6f). The different components are cemented by Fe-rich calcite (Fig. 6g). Dispersed muddy aggregates and framboidal pyrite occur occasionally throughout the churned matrix. Typical composition comprises 20–40% clay minerals, 20–30% quartz, > 50% carbonate (mainly bioclasts and blocky cement) and < 5% pyrite and other components.

Fig. 5 Distinctive petrographic features of the subfacies. Pictures from the split core. Scale bar indicates two centimetres. Blue arrows evidence epoxy resin. **a** Shaly facies (SF1). Yellow arrow points to mm thick rounded lenses, interpreted as bioturbational structures. **b** Carbonate-rich sandy facies (SF2). Yellow arrows show small ripples and thin, discontinuous, wavy laminae. White arrow indicates a thin, continuous, bioclastic lamina. **c** Sandy facies (SF3). Yellow arrows point to bioturbational structures. **d** Sandy facies (SF4). Yellow arrows evidence mud drapes. **e** Carbonate-rich sandy facies (SF4). Yellow arrows point to cm thick pyritized burrows. **f** Carbonate-rich sandy facies (SF2 and SF5). Yellow arrow evidences a SF5 patch. White arrow points to starved ripples (SF2). **g** 6 cm thick, authigenic, calcareous bed within the shaly facies. Cone-in-cone structures are not visible at macroscopic scale. **h** Boundary between shaly and carbonate-rich sandy facies (SF1 and SF4). Compacted, bioturbational lenses of SF4 appear within the shaly facies right below the boundary. **i** Carbonate-rich sandy facies (SF4). Yellow arrow evidences a brownish area associated to micritic siderite

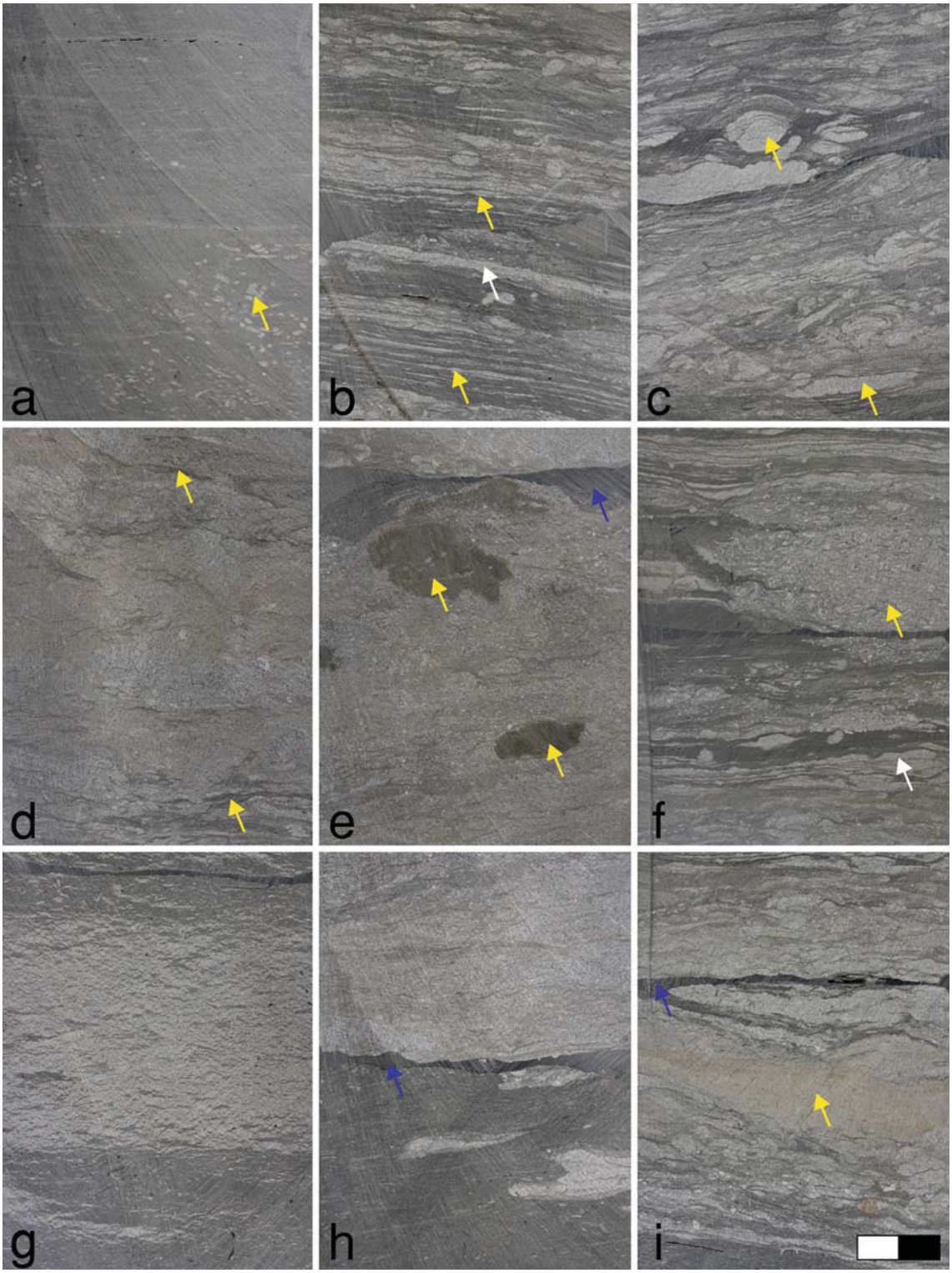

Clay minerals, carbonates and quartz are the main components of the lithological heterogeneity. The dominant composition of the different subfacies reflects a gradient, where mineralogy evolves from clay-rich (argillaceous; SF1) over quartz-rich (siliceous; SF3) towards carbonate-rich (calcareous; SF5). A general increase of bioturbation and average grain size, and a lightning of grey shade colours, is also observed from SF1 towards SF5.

4.2 Core description

The base of the BDM-B2 core (from 0.26 to 7.54 m) consist in a dark-grey, homogeneous, argillaceous and fine-grained lithology. It reflects the *shaly facies*, which is composed almost entirely of SF1. Sparse few-mm long bioclasts (mainly *Bositra*-shells) are typically enriched in 10–20 cm thick intervals. Six ammonites with preserved periostractum, and up to 7 cm in diameter, occur within a 70 cm interval (for location see Fig. 4; for ammonite species in the Opalinus Clay see Etter 1990; Reisdorf et al. 2014). A 3 mm thick pyrite horizon occurs at 1.72 m, and is traceable at the rock laboratory scale (e.g. Reisdorf et al. 2016). A 6 cm thick, bedding-parallel, calcareous bed was found contrasting with the rest of the lithology (Fig. 5g). The bed is composed of authigenic calcite crystals constituting small-scale cone-in-cone structures, and a few cm long shell fragments (Fig. 6h). Similar features were described in other Mont Terri drillcores (e.g. Bläsi et al. 1996; Reisdorf et al. 2016). The formation of cone-in-cone calcite is commonly interpreted as recrystallization associated with localized fluid overpressure, where bioclasts typically act as the carbonate source (e.g. Selles-Martinez 1994).

At core depth 7.54 m, a sharp erosional surface separates the shaly facies from the highly heterogeneous *carbonate-rich sandy facies* above (Fig. 5h). It shows about 70 cm of strongly bioturbated, calcareous-siliceous muddy sandstone with abundant bioclastic fragments (SF4). Two cm thick pyritized burrows are visible in this part. Upwards, a cm-scale heterogeneity is typically characterized by alternations of rather fine-grained, argillaceous material (SF2) and coarse-grained, cm thick bioclastic layers or patches (SF5). Siliceous-dominated subfacies (SF3 and SF4) occur also from time to time. The SF5 layers and patches typically exhibit sharp erosive bases. Alternations occur mostly within 5–30 cm thick successions. SF5 is particular to the carbonate-rich sandy facies and its occurrence decreases towards the top of the core. It totally disappears above 14.20 m. In contrast, an increase of SF4 is observed within the same depth interval. However, the upper part of the carbonate-rich sandy facies (from 11.54 to 14.00 m) is of bad core quality, consisting exclusively of cuttings. Diffuse impregnations of brownish, sideritic lime mud appear randomly within the SF4 and SF5 intervals (Fig. 5i). Similar features have been described by Bläsi et al. (1996), Lerouge et al. (2014) and Reisdorf et al. (2016) in further Opalinus Clay cores.

A rather continuous lithological transition separates the carbonate-rich sandy facies from the *sandy facies*. The facies boundary is set at core depth 14.30 m, where the calcareous-dominated lithology (SF4 and SF5) is gradually replaced by siliceous-dominated subfacies (SF3 and SF4). Above, the sandy facies presents successions evidencing smooth and gradual variations of the quartz:clay ratio. Typically, the successions are arranged in cm to dm thick coarsening- and fining-upward sequences, and characterized by alternations of SF3 and SF4. The degree of bioturbation influences the subfacies determination. SF2 occurs rarely. The intervals occupied by the individual subfacies tend to be thicker on average than in the carbonate-rich sandy facies underneath. Continuous intervals of SF3 can reach thicknesses of up to several dm and constitute the dominant part of the sandy facies. SF4 covers generally continuous intervals no longer than 10 cm. However, small-scale variations in the quartz:clay ratio occur also at the subfacies scale.

Fig. 6 Thin section microphotographs. **a** Characteristic plane-polarized light photomicrograph of the shaly facies (×25 magnification). Argillaceous fine mudstone typical of SF1. Yellow arrows indicate thin discontinuous lenses, probably compacted mud aggregates. Blue arrows show cracks and areas where the matrix was washed out during thin section preparation. **b** Characteristic plane-polarized light photomicrograph of SF2 (×25 magnification). Yellow arrow points to a bioclastic lamina; blue arrows indicate quartz-rich lenses and laminae; and white arrow shows an argillaceous lamina. The white layer in the centre is a crack due to thin section preparation. **c** Plane-polarized light photomicrograph of SF3 (×25 magnification). Yellow arrow evidences an individual, siliceous–calcareous lens within a homogenized silty to sandy matrix. Blue arrows point to diverse bioclasts. **d** Plane-polarized light photomicrograph of SF4 (×25 magnification). Yellow arrows show thin, wavy, mud laminae (mud drapes) within a homogenized silty to sandy matrix. **e** Cross-polarized light photomicrograph of typical components within SF4 (×100 magnification). Dark-blue-coloured components (yellow arrow) are sparitic Fe-calcite cement. Green arrow shows a muscovite flake. White to grey, angular to subangular components (black arrows) are quartz silt to sand grains. Blue arrow points to a bioclast. Pink arrow evidences an argillaceous floccule. Black and round components correspond to framboidal pyrite (red arrow). **f** Characteristic cross-polarized light photomicrograph of SF5 (×25 magnification). Main bioclasts are bivalve shell fragments (yellow arrow), crinoids (blue arrows) and sea urchin plates (red arrow). **g** Plane-polarized light photomicrograph of an accumulation of calcitic shell fragments (red-coloured; yellow arrow) and up to 0.5 mm thick, sparitic Fe-rich calcite crystals (blue-coloured; white arrow) within SF5 (×25 magnification). Quartz grains, muddy aggregates and framboidal pyrite constitute the matrix. **h** Characteristic cross-polarized light photomicrograph of the 6 cm thick authigenic, calcareous bed within the shaly facies (×50 magnification). Yellow arrow shows small-scale cone-in-cone structures and blue arrow indicates shell fragments

5 Geophysical and geochemical characterization

The most significant core logging (P-wave velocity, gamma density, Si, K, Al, Ca) and Rock-Eval (MinC and TOC) data were plotted against the lithology of the BDM-B2 core (Fig. 7).

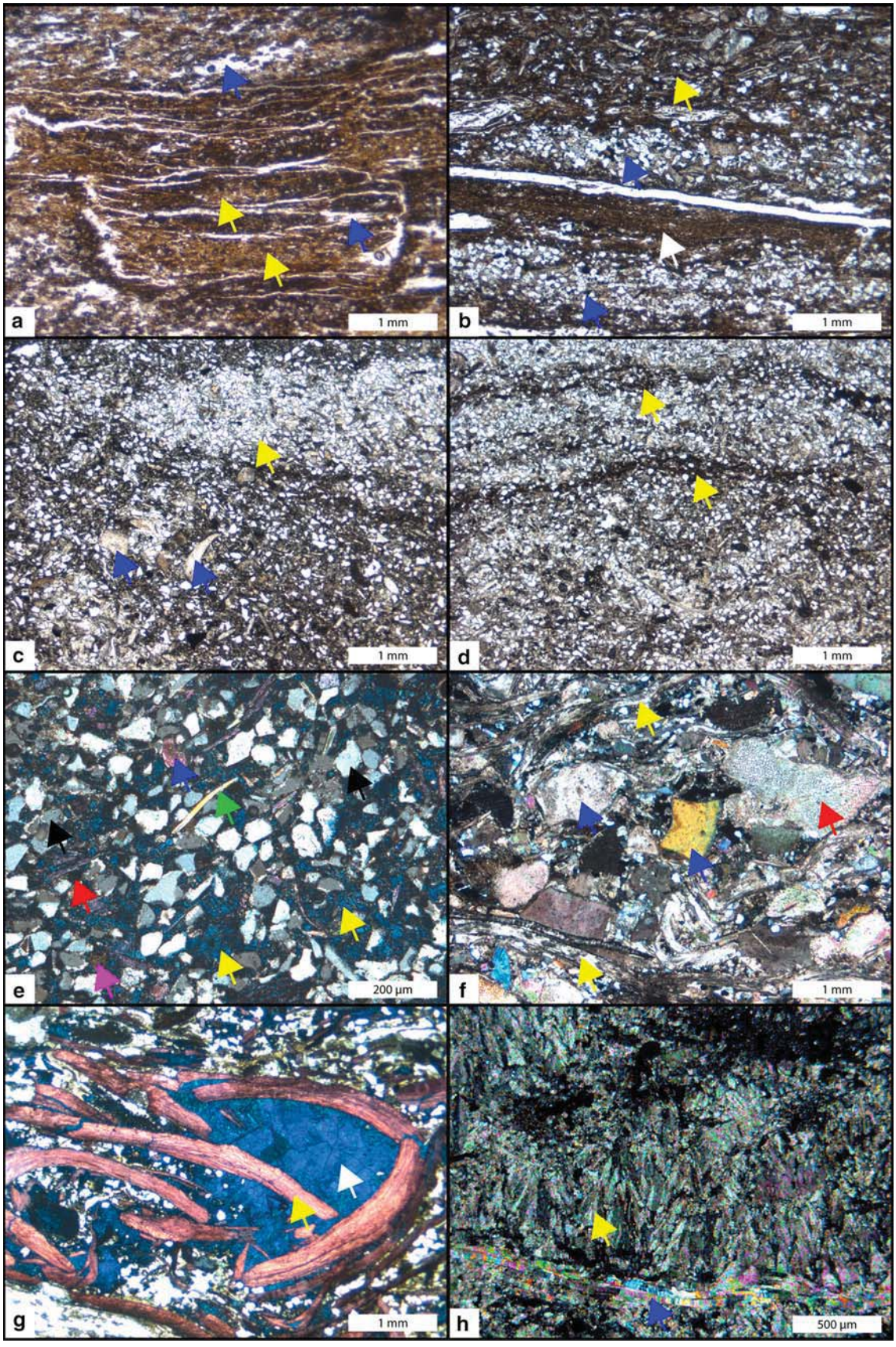

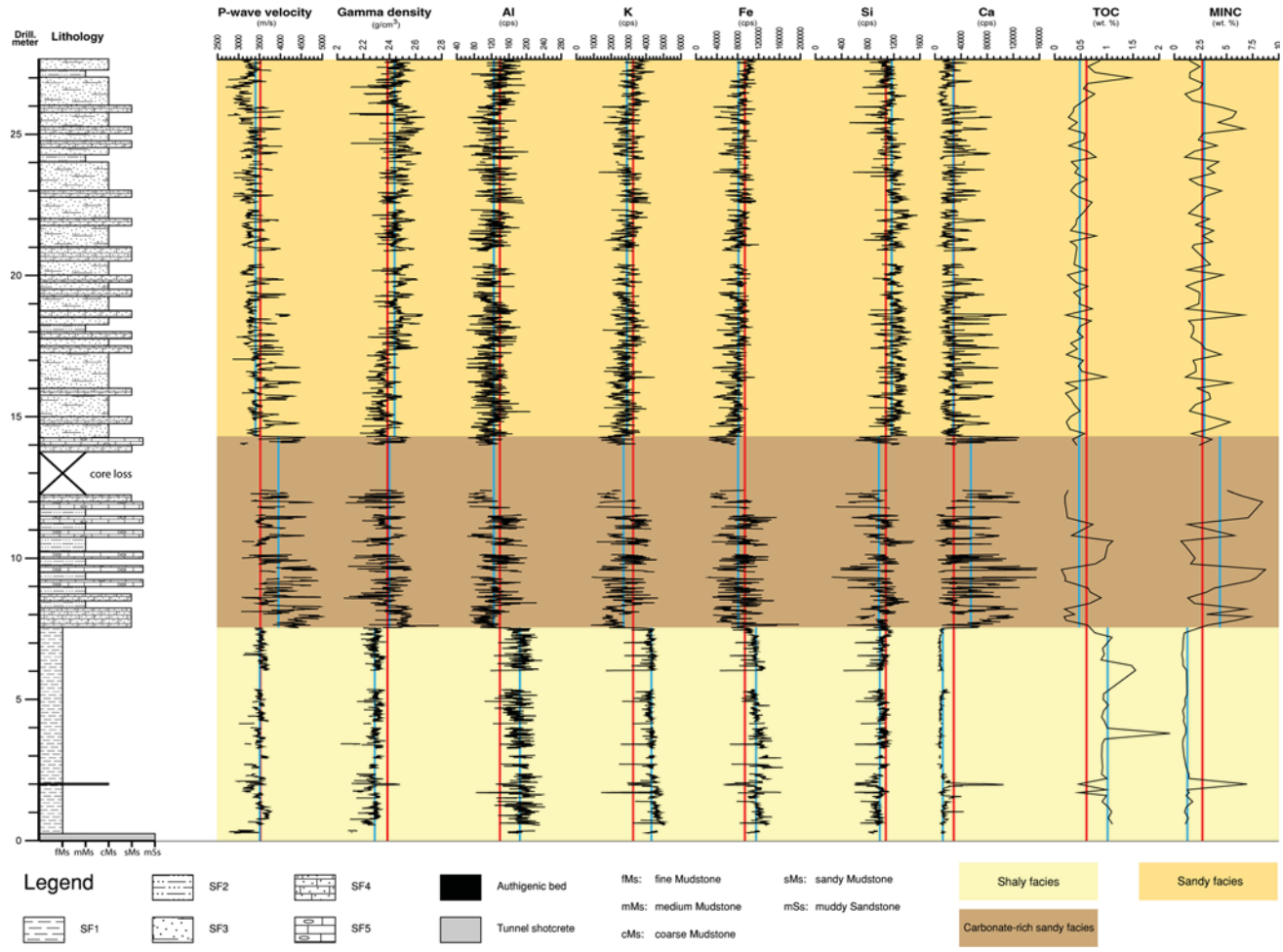

Fig. 7 P-wave velocity, gamma density, Al, K, Fe, Si, Ca, total organic carbon (TOC) and mineral organic carbon (MINC) are plotted towards the lithology of the BDM-B2 core. Major lithofacies are indicated in different brown shades. Continuous red lines indicate average values for each property, while blue lines indicate average values per lithofacies

5.1 Geophysical core logging data

P-wave velocity and gamma density records of the BDM-B2 core show a positive correlation, highlighting similar trends. Both signals display three major domains characterized by recurrent patterns. The lower section exhibits a low and uniform signal reflecting the homogeneous lithology of the shaly facies. Above 7.54 m, the signal presents high-amplitude fluctuations, typically showing the highest and some of the lowest values among the whole record. The range slightly decreases towards the top and shows a strong change at about 14.30 m. There is, however, a significant core loss between 11.54 and 14.00 m. Above 14.30 m, the variance decreases and tends to stabilize towards the top. The logging data reflect variations in lithology, such as mineralogy, grain size and porosity, which have a direct impact on the geophysical parameters. The more differentiated two successive lithologies are, the higher the change of variance between the two is. Because of the higher porosity, argillaceous material has a lower bulk density and thus, presents lower P-wave velocity and gamma density values. Well-cemented, calcareous and siliceous materials has a lower porosity and shows higher P-wave velocity and gamma density values. Consequently, the succession with the highest variance (from 7.54 to 14.30 m) reflects the highly heterogeneous carbonate-rich sandy facies with intercalated argillaceous material (SF2) and calcareous-siliceous material (SF4 and SF5). A lower variance in the uppermost section reflects alternations of less differentiated material, typically intervals composed of SF3 and SF4.

5.2 Geochemical core logging data

The geochemical variations of Al, Si, Fe, K and Ca along the BDM-B2 core present three distinctive domains corroborating the three major lithofacies along the core. The Ca record is particularly significant and shows similar

patterns as observed in the geophysical records: low and uniform signal in the shaly facies; signal with high variance in the carbonate-rich sandy facies; and signal with medium-range variance in the sandy facies. In fact, calcium is a direct indicator for the carbonate content within the Opalinus Clay, and its variation along the core reflects the amount of carbonate cement and bioclasts. Al and K records inversely correlate with the Ca record. They reflect the average clay content within the core sections, as micas, feldspars and other minor components are negligible. The Fe record tends to show a similar trend even though iron occurs in Fe-rich calcite, siderite and pyrite in addition to clay minerals. Higher Fe peak values, however, reflect intervals rich in pyrite (disseminated or concretionary). The Si record shows also three domains, where the higher values are found in the sandy facies. It is thus a good indicator for relative changes in quartz content with respect to carbonate and clay minerals content. The geochemical core logging data show lithological variations at both, lithofacies and subfacies scale.

5.3 Rock-Eval pyrolysis data

TOC and MinC records are inversely correlated and reflect both the lithological variations along the BDM-B2 core of the quite homogeneous shaly facies, the heterogeneous carbonate-rich sandy facies and the less-differentiated and generally coarser sandy facies. The highest TOC values were measured in the shaly facies and, more generally, in fine-grained and clay-rich intervals. Coarse-grained and carbonate-rich intervals present much lower TOC values, particularly in SF5 intervals. The MinC data, which are very consistent with the Ca record, show inverse trends.

According to the HI vs. OI diagram, three distinctive patterns representing the three lithofacies are distinguished (Fig. 8a). The organic matter of the shaly facies suggests mainly type II kerogen. The carbonate-rich sandy facies reflects mixed types II and III kerogen, while the sandy facies suggests mainly type III kerogen.

The data inferred by the S2 vs. TOC diagram suggest a type II kerogen for the shaly facies (HI = 399 mg/g TOC), mixed types II and III kerogen for the carbonate-rich sandy facies (HI = 218 mg/g TOC), and a type III kerogen for the sandy facies (HI = 141 mg/g TOC; Fig. 8b). In order to quantify the matrix effect, an x-intercept of 0.58 wt% TOC was found for the shaly facies, 0.13 wt% TOC for the carbonate-rich sandy facies and 0.03 wt% TOC for the sandy facies (Fig. 8b). Hence, the Rock-Eval samples support the petrographic analyses by implying a relative

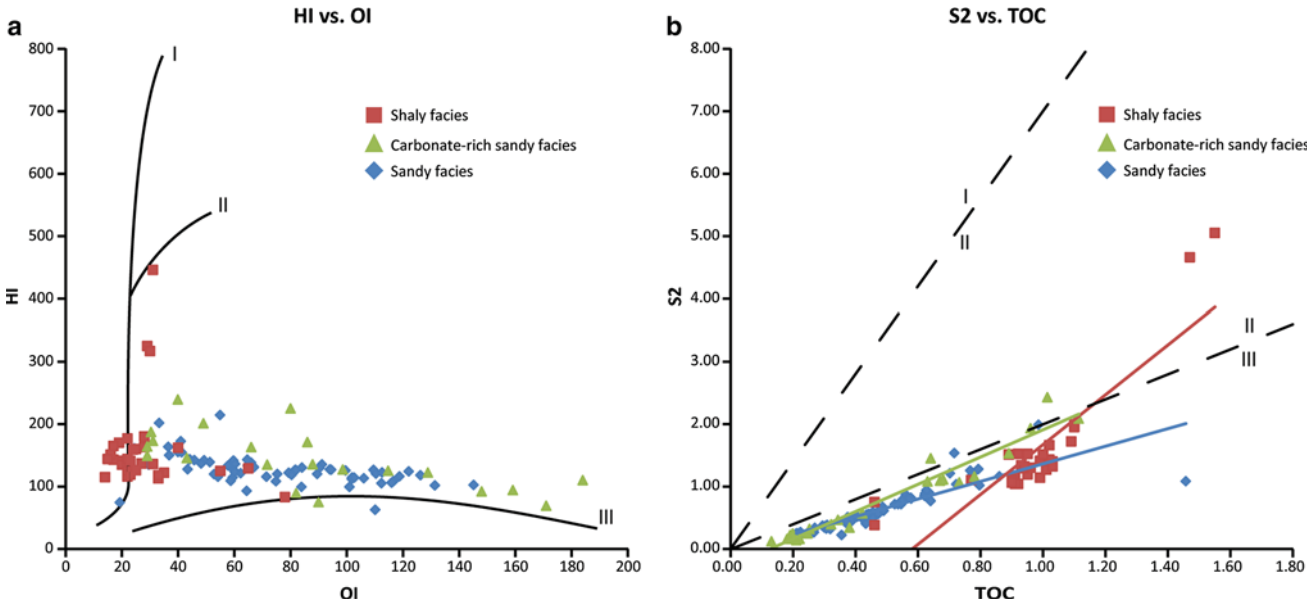

Fig. 8 **a** HI vs. OI diagram. Rock-Eval samples are referenced by lithofacies. Continuous lines indicate maturity paths of the different kerogen types. Three different patterns are identified for each major lithofacies. **b** S2 vs. TOC diagram. Rock-Eval samples are referenced by lithofacies. Regression lines are drawn for each major lithofacies and their equations are given: shaly facies (in red): $y = 3.9904x - 2.3188$ ($r = 0.85$); carbonate-rich sandy facies (in green): $y = 2.1823x - 0.2745$ ($r = 0.97$) and sandy facies (in blue): $y = 1.4087x - 0.045$ ($r = 0.86$), where r is the coefficient of correlation. The HI is inferred from the regression equation and corresponds to 100 times the slope. The dashed line marked I/II represents a HI of 700 mg HC/g TOC and the dashed line marked II/III represents a HI of 200 mg HC/g TOC. The I/II line corresponds to the minimum slope characterizing type I kerogen and the II/III line corresponds to the minimum slope characterizing type II kerogen (see Langford and Blanc-Valleron 1990). The matrix effect is indicated by a positive x-intercept of the regression lines and the position of the intercept is a measure of the amount of adsorption

decrease in the average clay content, from the shaly facies, over the carbonate-rich sandy facies, to the sandy facies.

6 Discussion and interpretation

6.1 Small-scale facies heterogeneity in the Opalinus Clay

This multi-proxy analytical study supports previous lithological descriptions conducted in the Mont Terri rock laboratory by highlighting the occurrence of three major lithofacies (e.g. Bossart and Thury 2008). It demonstrates also high intra-facies heterogeneity. To prove the lateral validity of the subfacies classification inferred from the single BDM-B2 core, a comparison to the petrographic study of a tunnel niche can be performed. Müller and Jaeggi (2012) described four so-called subtypes (subtypes A–D) within the TT-niche (Fig. 3), which covers the carbonate-rich sandy facies to sandy facies transition. They described subtype A as dark argillaceous laminated clay; subtype B as bioclastic limestone; subtype C as grey silty clay, relatively homogeneous; and subtype D as intercalation of silty clay and black clay. As TT-niche subtypes and BDM-B2 subfacies present strong similarities, the following equivalences are suggested: subtype A = SF2; subtype B = SF5; subtype C = SF4; and subtype D = SF3. Hence, a lateral validity of the subfacies classification at the rock laboratory scale can be assumed. The examination of further drillcore descriptions crossing the same facies transition (e.g. Bläsi et al. 1991, 1996; Reisdorf et al. 2016) supports this assumption.

Unravelling small-scale lithological heterogeneity through the definition of subfacies provides conspicuous arguments to better define transitional lithofacies boundaries. Typically, the distribution of the carbonate-rich sandy facies within the rock laboratory can be associated to the occurrence of SF5. Further applications may include the prediction of various rock mechanical and petrophysical parameters that are strongly influenced by lithological and (micro)fabric variations, such as failure strength (e.g. Kaufhold et al. 2013), micro-porosity (e.g. Houben et al. 2014) or anisotropic diffusion (e.g. Van Loon et al. 2004).

6.2 Multi-proxy facies analysis: an efficient tool for rock characterization

The present study demonstrates that lithological variation in the Opalinus Clay can be efficiently recorded by geophysical and geochemical core logging. These methods allowed the identification of lithological patterns at two distinctive scales. While main signal regimes are associated to major lithofacies (10^0–10^1 m), small-scale variance reflects subfacies variations (10^{-1}–10^{-2} m). Previous studies showed already correlations of geophysical parameters with lithological variations in the Opalinus Clay. For example, Bläsi et al. (1996) compared gamma ray, electrical resistivity, caliper and sonic logs with lithology of core sections and tectonic structures. Some correlations showed consistent results, such as the increase of electrical resistivity and sonic velocity in layers strongly cemented by calcite. However, the authors could not establish reliable correlations arguing that the inconsistency of several log signatures cannot be explained by true lithological changes. Wonik (1996) identified in gamma ray and electrical resistivity logs, three lithofacies trends expressing either increase or decrease in clay minerals, quartz and carbonate content, as well as changes in porosity. Reisdorf et al. (2016) combined gamma ray borehole logs with XRD measurements in order to estimate clay mineral content along several sections of a 250 m-deep well drilled at Mont Terri. The authors identified distinctive signal responses for each major lithofacies and the clay content estimate showed coherent results. They also noticed the importance of geophysical criteria to constrain intra-formational lithological transitions. With the present geophysical core logging, correlation of geophysical proxies with defined lithofacies could be confirmed through direct core log correlations.

According to the petrographic observations, the Opalinus Clay is characterized by three major mineralogical components: clay minerals, quartz and carbonate. Lithological heterogeneity is thus represented by different ratios of these major components. The geochemical records reveal to be convenient for detecting these changes. Although direct association between elemental and mineralogical compositional variation is not always appropriate due to the incorporation of certain elements in various minerals, the results show coherent correlations. For instance, the MinC and Ca records correlate well with the petrographic-based, total carbonate estimate. True correlations between Rock-Eval MinC values and XRD total carbonate contents have already been demonstrated in different settings by Jiang et al. (2017).

6.3 Depositional setting

Several studies outline that the Opalinus Clay was deposited during late Toarcian to early Aalenian times in a shallow-marine epicontinental sea covering Central Europe (e.g. Ziegler 1990; Wetzel and Allia 2003). Petrographic observations suggest that lithological diversity within the Opalinus Clay is mainly influenced by clastic delivery (occurrence of silty/sandy laminae, lenses and beds), presence of infaunal organisms (degree of bioturbation and presence of autochthonous bioclasts) and formation of

diagenetic features (carbonate and pyritic concretions, cone-in-cone structures). Examination of lithological descriptions in the literature (Bläsi 1987; Matter et al. 1987, 1988; Bläsi et al. 1991, 1996; Nagra 2001; Wetzel and Allia 2000, 2003; Müller and Jaeggi 2012; Reisdorf et al. 2016) suggests the same factors of influence. Hence, the facies distribution recorded by the BDM-B2 core allows the identification of some depositional processes and their link towards depositional environments (Fig. 9).

Classical interpretation of fine-grained, argillaceous sediments, such as the *shaly facies*, suggests sediment accumulation by suspension settling (muddy floccules or aggregates), in rather low energy environments, and typically situated below the storm-wave base (e.g. Potter et al. 2005). However, Schieber et al. (2007) demonstrated that some apparently homogeneous-looking mudstones might reflect current-transport of mud aggregates, suggesting hence a depositional environment more energetic than previously supposed. The typical lenticular microfabric of these mudstones (see also Schieber et al. 2010) could however, not be recognized in SF1 thin sections. Occasional finds of ammonites suggest water depths from a few dozens to several hundred metres (e.g. Westermann 1982). Based on paleoecological and sedimentological analyses, Etter (1990) proposed an average water depth for the lower Opalinus Clay (similar to the shaly facies) of roughly 60–100 m. However, Wetzel and Allia (2003) suggested deposition at about 50 m depth. The poor diversity of ammonite species (Reisdorf et al. 2014) suggest water depths comparable to those proposed by Wetzel and Allia (2003). Rather rare bioturbational structures combined to the overall poor content of bioclasts, nuanced by intervals enriched in *Bositra*-shells, typical of oxygen-depleted paleoenvironments (e.g. Etter 1996), point to the prevalence of dysaerobic conditions at the seafloor. Bio- and taphofacies analyses of the lower Opalinus Clay in northern Switzerland provided similar interpretations (e.g. Etter 1990, 1996). Dysaerobic bottom-water conditions are supported by relatively higher TOC content and the identification of type II kerogen, which are typical for oxygen-deficient environments in moderately to deep marine settings (e.g. McCarthy et al. 2011).

In contrast to the shaly facies, the carbonate-rich sandy and sandy facies are both characterized by higher silt and sand contents. The provenance of the sediment is however still discussed. Wetzel et al. (2003) mentioned the Bohemian Massif, the London-Brabant Massif and the Rhenish Massif, and subordinately the Alemannic Islands as possible sources. All these locations indicate deposition at several tens to hundred km from the delivery source (e.g. Etter 1990; Wetzel et al. 2003). Nonetheless, the quartz grains in the BDM-B2 succession never exceed 150 µm, suggesting that suspension load might still be the main transport agent. Such sediment transport can cover long distances.

The *carbonate-rich sandy facies* shows mainly alternations of SF2 and SF5. Numerous starved ripples and thin discontinuous silt laminae in SF2 point to limited sediment supply. This subfacies is associated to rather distal sediment deposition close to, or below the storm-wave base, in storm-wave-dominated environments (e.g. Wetzel and Allia 2003). It reflects the background sedimentation of the carbonate-rich sandy facies. SF5 represents smaller intervals induced by energetic events. This subfacies contains large bioclastic fragments and much smaller quartz grains and mud aggregates, suggesting deposition within the same hydraulic regime (see also Müller and Jaeggi 2012). It evidences sharp erosive bases and occurs as cm thick layers or patches, arguing for transport by erosive currents and possible deposition as pot and gutter casts under storm influence (e.g. Myrow 1992). The large bioclasts in SF5 contrast with the size of the bioclasts observed in other subfacies. Furthermore, there is no evidence of carbonate-rich sandy facies further to the east. This facies might thus point to a local origin. Temporary topographic swells composed of coarser sediments may have allowed the development of local short-lived carbonate factories situated above the storm-wave base. On the top of the swells, stronger currents prevented finer sediments to accumulate and provided prolonged periods of stable conditions,

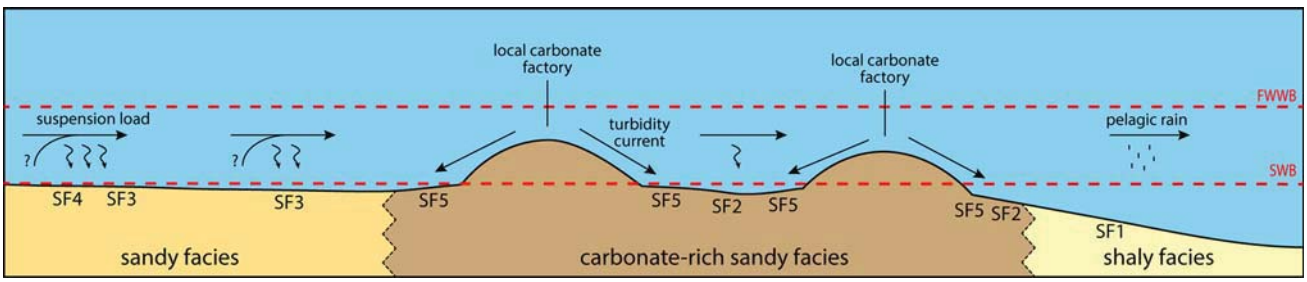

Fig. 9 Schematic epicontinental basin presenting idealized spatial distribution of main depositional environments of the three major lithofacies within the Mont Terri Opalinus Clay. Potential depositional environments of subfacies are also indicated. *FWWB* fair-weather wave base, *SWB* storm wave base

favouring faunal colonization of e.g. echinoderms and bivalves. It likely provided a substrate for the development of such carbonate factory in an overall muddy environment. The bioclastic material (SF5) was transported by storm-induced turbidity currents from the top of the swells towards adjacent depocenters. Topographical variations of a few tens dm were probably sufficient to induce these phenomena. Wetzel and Meyer (2006) discussed similar short-lived swells in their interpretation of crinoid deposits surrounded by mudstones in the Opalinus Clay. Furthermore, the sideritic impregnations within the carbonate-rich sandy facies (mostly in SF5) suggest periods of reduced sedimentation rates between two sporadic storm events (e.g. Lerouge et al. 2014).

The *sandy facies* is characterized by a high degree of bioturbation and by the presence of small autochthonous bioclasts (see also Bläsi et al. 1996), suggesting aerobic benthic conditions. Larger bioclasts (echinoderms and bivalves) are mainly present as broken fragments, arguing for high-energy transport. Wavy bedding and small ripple marks as in SF4, are often associated to reworking by bottom currents (e.g. Potter et al. 2005). The strongly bioturbated aspect of SF4 suggests colonization by infaunal organisms between storm events (e.g. Macquaker et al. 2007). Starved ripples in SF3 reflect limited silt and sand supply, likely related to decreasing water energy during late phases of storm events (e.g. Wetzel and Allia 2003). The lenticular fabric of SF3 is mostly attributed to compacted bioturbational structures. There is no evidence of thick sand beds with hummocky structures in the Mont Terri area, such as described by Wetzel and Allia (2003) in northern Switzerland. Yet, such observations would constitute a hint for deposition above the storm wave base (e.g. Dott and Bourgeois 1982). Nonetheless, presence of post storm-produced features and absence of fossil ammonites within the sandy facies suggest a relatively shallow water depth, probably a few tens of metres. Wetzel and Allia (2003) interpreted the Opalinus Clay as successive tempestites accumulating at water depths of about 20 m. A relatively high amount of silt and sand in the sandy facies might suggest closer proximity towards the sediments delivery source than the previous facies. This hypothesis is supported by the presence of type III kerogen in the sandy facies, although the overall TOC therein is low. However, climatic variations or changes in sediment transfer patterns cannot be ruled out as the main factors controlling sediment distribution within the depositional basin.

The studied core succession shows the sedimentary record deposited in an epicontinental sea setting affected by temporal changes in sedimentation rate, water depth and seafloor topography. During the Lower Jurassic, an extensional stress field due to the opening of the Tethys and the Atlantic Ocean induced the reactivation of pre-existing structures in the crystalline basement (Wetzel et al. 2003). This extensional episode was associated with the formation of fault bounded tilted blocks, which led by differential subsidence to the development of local sub-basins. The resulting depositional area was thus morphologically differentiated into swells and depressions, with local environmental parameters influencing sediment deposition (e.g. Matter et al. 1987, 1988; Wetzel and Allia 2000, 2003; Wetzel and Meyer 2006). The lithofacies architecture at Mont Terri differs from what has been described further to the east. There, the Opalinus Clay shows five to six, laterally correlatable sub-units (Bläsi 1987; Matter et al. 1987, 1988). The formation was interpreted as recording an overall shallowing-upward trend, characterized by a general increase in quartz and carbonates with respect to clay minerals. The BDM-B2 succession also reflects a shallowing-upwards trend. At the rock laboratory scale, the Opalinus Clay evidences two successive coarsening-upwards successions, both from a shaly facies towards a sandy facies. The second coarsening-upwards sequence does however not show any carbonate-rich sandy facies (e.g. Bläsi et al. 1991). One possible reason therefor involves the absence of local carbonate factories during deposition time. Nonetheless, the boundary is described as being transitional, with the occurrence of thin silt lenses (SF2-like) in the upper part of the upper shaly facies (Reisdorf et al. 2016). By extrapolation, the lithofacies distribution within the Mont Terri rock laboratory might be interpreted as two successive shallowing-upward sequences. The transitional boundary between the lower sandy facies and the upper shaly facies would reflect a flooding surface indicating a relative deepening of the sea level, characterized by an increase of the accommodation space. Seen the enhanced subsidence rates during the Aalenian, this increase in the water depth might be the result of a local subsidence pulse, likely reflecting the reactivation of pre-existing structures. A few tens of km west from Mont Terri, in Franche-Comté (France), the 130–160 m thick Opalinus Clay is replaced by less than 3 m of sandy limestones (Calcaires sableux d'Aresches; Contini 1970). This abrupt lithological change might be a further hint for a depositional setting largely influenced by synsedimentary tectonics in the Mont Terri area, probably producing the differing lithofacies.

7 Conclusions

The multi-proxy analytical study of the BDM-B2 core demonstrates that lithological variation within the Opalinus Clay can be unravelled by different methods. The petrographic investigation revealed the presence of three major lithofacies: a shaly facies, a carbonate-rich sandy facies

and a sandy facies. It also proves high intra-facies heterogeneity, which resulted into the definition of five subfacies (SF1–SF5). The geophysical and geochemical core logging recorded lithological variability at two different scales. While main signal regimes were associated to major lithofacies (10^0–10^1 m), small-scale variance reflected subfacies variations (10^{-1}–10^{-2} m). The Rock-Eval analyses identified three distinctive patterns reflecting the major lithofacies. Type II kerogen for the shaly facies; mixed types II and III kerogen for the carbonate-rich sandy facies; and type III kerogen for the sandy facies were identified.

The BDM-B2 lithofacies succession is interpreted as a shallowing-upward sequence. It was recorded in an epicontinental sea characterized by relative shallow water depths and influenced by storm events. Facies variations reflect changes in depositional, environmental, relative sea level and diagenetic conditions. The sediments were deposited in an area morphologically differentiated into swells and depressions. The shaly facies was deposited into comparably deeper water depths, where level dysaerobic bottom-water prevailed. The carbonate-rich sandy facies suggests the existence of local carbonate factories providing bioclastic material for re-deposition under storm influence into adjacent depocenters. The sandy facies indicate high-energy transport, reworking by bottom currents, and aerobic conditions at the seafloor. The lithofacies architecture at Mont Terri differs from the Opalinus Clay successions described further east. This strong W-E lateral variability is seen as reflecting synsedimentary tectonics and differential subsidence of the depositional area into local sub-basins.

Acknowledgements The authors thank Paul Bossart (Swisstopo) and André Strasser (University of Fribourg) for having launched the present project. Flavio Anselmetti and Hendrik Vogel (University of Bern) are sincerely acknowledged for their help with MSCL and XRF core logging, respectively, as well as Thierry Adatte (University of Lausanne) for providing Rock-Eval measurements. The technical teams of the University of Fribourg and the Mont Terri Project are warmly thanked for their technical and logistic support. Jens Becker (Nagra), the reviewers Andreas Wetzel (University of Basel), Bernhard Hostettler and Ursula Menkveld-Gfeller (Natural History Museum Bern), and the editor Silvia Spezzaferri (University of Fribourg) are thanked for their helpful comments on an earlier version of the manuscript. Finally, the partners involved in the SO-Experiment of the Mont Terri Project (Swisstopo and BGR) and the University of Fribourg are acknowledged for their financial contribution.

References

Bläsi, H.-R. (1987). Lithostratigraphie und Korrelation der Doggersedimente in den Bohrungen Weiach, Riniken und Schafisheim. *Eclogae Geologicae Helvetiae, 80,* 415–430.

Bläsi, H.-R., Moeri, A., & Bossart, P. (1996). *Results of the phase 1 drilling campaign*. Mont Terri technical report, TR 96-01, Federal Office of Topography (swisstopo), Wabern, Switzerland. http://www.mont-terri.ch.

Bläsi, H.-R., Peters, T., & Mazurek, M. (1991). *Der Opalinus-Ton des Mt. Terri (Kanton Jura): Lithologie, Mineralogie und phyiko-chemische Gesteinsparameter*. Nagra Interner Bericht, NTB 90-60, Nagra, Wettingen, Switzerland. http://www.nagra.ch.

Bossart, P., Bernier, F., Birkholzer, J., Bruggeman, C., Connolly, P., Dewonck, S., et al. (2017). Mont Terri rock laboratory, 20 years of research: Introduction, site characteristics and overview of experiments. *Swiss Journal of Geosciences, 110,* 3–22.

Bossart, P., & Thury, M. (2008). *Mont Terri Rock Laboratory. Project, programme 1996 to 2007 and results.* Reports of the Swiss Geological Survey, No. 3, Federal Office of Topography (swisstopo), Wabern, Switzerland. http://www.mont-terri.ch.

Burkhalter, R. M. (1996). Die Passwang-Alloformation (unteres Aalénien bis unteres Bajocien) im zentralen und nördlichen Schweizer Jura. *Eclogae Geologicae Helvetiae, 89,* 875–934.

Caër, T., Maillot, B., Souloumiac, P., Leturmy, P., Frizon de Lamotte, D., & Nussbaum, C. (2015). Mechanical validation of balanced cross-sections: The case of the Mont Terri anticline at the Jura front (NW Switzerland). *Journal of Structural Geology, 75,* 32–48.

Contini, D. (1970). *L'Aalénien et le Bajocien du Jura Franc-Comtois*. Ph.D. dissertation, University of Besançon, Besançon, France

Dickson, J. A. D. (1965). A modified staining technique for carbonates in thin section. *Nature, 205,* 587.

Dott, R. H., & Bourgeois, J. (1982). Hummocky stratification: Significance of its variable bedding sequences. *Geological Society of American Bulletin, 93,* 663–680.

Espitalié, J., Deroo, G., & Marquis, F. (1985). La pyrolyse Rock-Eval et ses applications; première et deuxième parties. *Revue de l'Institut Français du Pétrole, 40,* 563–579. **(755–784)**.

Etter, W. (1990). *Paläontologische Untersuchungen im unteren Opalinuston der Nordschweiz*. Ph.D. dissertation, University of Zurich, Zurich, Switzerland

Etter, W. (1996). Pseudoplanktonic and benthic invertebrates in the Middle Jurassic Opalinum Clay, northern Switzerland. *Palaeogeography, Palaeoclimatology, Palaeoecology, 126,* 325–341.

Freivogel, M., & Huggenberger, P. (2003). Modellierung bilanzierter Profile im Gebiet Mont Terri-La Croix (Kanton Jura). In P. Heitzmann, & J.-P. Tripet (Eds.), *Mont Terri Project—Geology, Paleohydrology and stress field of the Mont Terri region* (vol. 5). *Geology series.* Federal Office for Water and Geology (FOWG). http://www.mont-terri.ch.

Hostettler, B., Reisdorf, A. G., Jaeggi, D., Deplazes, G., Bläsi, H.-R., Morard, A., et al. (2017). Litho- and biostratigraphy of the Opalinus Clay and bounding formations in the Mont Terri rock laboratory (Switzerland). *Swiss Journal of Geosciences, 110,* 22–37.

Houben, M. E., Desbois, G., & Urai, J. L. (2014). A comparative study of representative 2D microstructures in Shaly and Sandy facies of Opalinus Clay (Mont Terri, Switzerland) inferred form BIB-SEM and MIP methods. *Marine and Petroleum Geology, 49,* 143–161.

Jiang, C., Chen, Z., Lavoie, D., Percival, J. B., & Kabanov, P. (2017). Mineral carbon MinC(%) from Rock-Eval analysis as a reliable and cost-effective measurement of carbonate contents in shale source and reservoir rocks. *Marine and Petroleum Geology, 83,* 184–194.

Kaufhold, A., Gräsle, W., Plischke, I., Dohrmann, R., & Siegesmund, S. (2013). Influence of carbonate content and micro fabrics on the failure strength of the sandy facies of the Opalinus Clay from Mont Terri (Underground Rock Laboratory). *Engineering Geology, 156,* 111–118.

Langford, F. F., & Blanc-Valleron, M.-M. (1990). Interpreting Rock-Eval pyrolysis data using graphs of pyrolizable hydrocarbons vs.

total organic carbon. *American Association of Petroleum Geologists Bulletin, 74,* 799–804.

Lazar, O. R., Bohacs, K. M., Macquaker, J. H. S., Schieber, J., & Demko, T. M. (2015). Capturing key attributes of fine-grained sedimentary rocks in outcrops, cores, and thin sections: nomenclature and description guidelines. *Journal of Sedimentary Research, 85,* 230–246.

Lerouge, C., Grangeon, S., Claret, F., Gaucher, E., Blanc, P., Guerrot, C., et al. (2014). Mineralogical and isotopic record of diagenesis from the Opalinus Clay formation at Benken, Switzerland: implications for the modeling of pore-water chemistry in a clay formation. *Clays and Clay Minerals, 62,* 286–312.

Macquaker, J. H. S., Taylor, K. G., & Gawthorpe, R. L. (2007). High-resolution facies analyses of mudstones: Implications for paleoenvironmental and sequence stratigraphic interpretations of offshore ancient mud-dominated successions. *Journal of Sedimentary Research, 77,* 324–339.

Matter, A., Peters, T., Bläsi, H.-R., Meyer, J., Ischi, H., & Meyer, C. (1988). *Sondierbohrung Weiach—Geologie*. Nagra Technischer Bericht, NTB 86-01, Nagra, Wettingen, Switzerland. http://www.nagra.ch.

Matter, A., Peters, T., Isenschmid, C., Bläsi, H.-R., & Ziegler, H.-J. (1987). *Sondierbohrung Riniken—Geologie*. Nagra Technischer Bericht, NTB 86-02, Nagra, Wettingen, Switzerland. http://www.nagra.ch.

Mazurek, M. (2011). *Aufbau und Auswertung der Gesteinsparameter—Datenbank für Opalinuston, den Braunen Dogger, Effinger Schichten und Mergel-Formation des Helvetikums*. Nagra Arbeitsbericht, NAB 11–20, Nagra, Wettingen, Switzerland. http://www.nagra.ch,

McCarthy, K., Rojas, K., Niemann, M., Palmowski, D., Peters, K., & Stankiewicz, A. (2011). Basic petroleum geochemistry for source rock evaluation. *Oilfield Review, 23,* 32–43.

Müller, P., & Jaeggi, D. (2012). *SO experiment: Sedimentary structure in the sandy facies of the Opalinus Clay at Mont Terri rock laboratory*. Mont Terri technical note, TN 2012-45, Federal Office of Topography (swisstopo), Wabern, Switzerland. http://www.mont-terri.ch.

Myrow, P. M. (1992). Pot and gutter casts from the Chapel Island Formation, Southeast Newfoundland. *Journal of Sedimentary Petrology, 62,* 992–1007.

Nagra. (2001). *Sondierbohrung Benken Untersuchungsbericht*. Nagra Technischer Bericht, NTB 00-01, Nagra, Wettingen, Switzerland. http://www.nagra.ch.

Nagra. (2002). *Projekt Opalinuston: Synthese der geowissenschaftlichen Untersuchungsergebnisse. Entsorgungsnachweis für abgebrannte Brennelemente, verglaste hochaktive sowie langlebige mittelaktive Abfälle*. Nagra Technischer Bericht, NTB 02-03, Nagra, Wettingen, Switzerland. http://www.nagra.ch

Nussbaum, C., Bossart, P., Amman, F., & Aubourg, C. (2011). Analysis of tectonic structures and excavation induced fractures in the Opalinus Clay, Mont Terri underground rock laboratory (Switzerland). *Swiss Journal of Geosciences, 104,* 187–210.

Potter, P. E., Maynard, J. B., & Depetris, P. J. (2005). *Mud and mudstones: Introduction and overview*. New York: Springer.

Reineck, H.-E., & Wunderlich, F. (1968). Classification and origin of flaser and lenticular bedding. *Sedimentology, 11,* 99–104.

Reisdorf, A.G., Hostettler, B., Jaeggi, D., Deplazes, G., Bläsi, H.-R., Morard, A., Feist-Burkhardt, S., Waltschew, A., Dietze, V., & Menkveld-Gfeller, U. (2016). *Litho- and biostratigraphy of the 250 m-deep Mont Terri BDB-1 borehole through the Opalinus Clay and bounding formations, St-Ursanne, Switzerland*. Mont Terri technical report, TR 2016-02, Federal Office of Topography (swisstopo), Wabern, Switzerland. http://www.mont-terri.ch.

Reisdorf, A.G., Hostettler, B., Waltschew, A., Jaeggi, D., & Menkveld-Gfeller, U. (2014). *SO experiment: Biostratigraphy of the basal part of the Opalinus-Ton of the Mont Terri rock laboratory, Switzerland*. Mont Terri technical note, TN 2013-111, Federal Office of Topography (swisstopo), Wabern, Switzerland. http://www.mont-terri.ch

Reisdorf, A. G., Wetzel, A., Schlatter, R., & Jordan, P. (2011). The Staffelegg Formation: a new stratigraphic scheme for the Early Jurassic of northern Switzerland. *Swiss Journal of Geosciences, 104,* 97–146.

Schieber, J., Southard, J. B., & Schimmelmann, A. (2010). Lenticular shale fabric resulting from intermittent erosion of water-rich muds—Interpreting the rock record in the light of recent flume experiments. *Journal of Sedimentary Research, 80,* 119–128.

Schieber, J., Southard, J., & Thaisen, K. (2007). Accretion of mudstone beds from migrating floccule ripples. *Science, 318,* 1760–1763.

Selles-Martinez, J. (1994). New insights in the origin of cone-in-cone structures. *Carbonates and Evaporites, 9,* 172–186.

Thury, M., & Bosart, P. (1999). The Mont Terri rock laboratory, a new international research project in a Mesozoic shale formation, in Switzerland. *Engineering Geology, 52,* 347–359.

Van Loon, L. R., Soler, J. M., Müller, W., & Bradbury, M. H. (2004). Anisotropic diffusion in layered argillaceous rocks: A case study with Opalinus Clay. *Environmental Science and Technology, 38,* 5721–5728.

Westermann, G. E. G. (1982). The connecting rings of Nautilus and Mesozoic ammonoids: Implications for ammonoid bathymetry. *Lethaia, 15,* 373–384.

Wetzel, A., Allenbach, R., & Allia, V. (2003). Reactivated basement structures affecting the sedimentary facies in a tectonically "quiescent" epicontinental basin: An example from NW Switzerland. *Sedimentary Geology, 157,* 153–172.

Wetzel, A., & Allia, V. (2000). The significance of hiatus beds in shallow-water mudstones: An example from the Middle Jurassic of Switzerland. *Journal of Sedimentary Research, 70,* 170–180.

Wetzel, A., & Allia, V. (2003). Der Opalinuston in der Nordschweiz: Lithologie und Ablagerungsgeschichte. *Eclogae Geologicae Helvetiae, 96,* 451–469.

Wetzel, A., & Meyer, C. A. (2006). The dangers of high-rise living on a muddy seafloor: An example of crinoids from shallow-water mudstones (Aalenian, northern Switzerland). *Palaios, 21,* 155–167.

Wonik, T. (1996). Geophysikalische Untersuchungen. In Geologisches Landesamt Baden-Württemberg (Eds.), *Die Grenzziehung Unter-/Mitteljura (Toarcium/Aalenium) bei Wittnau und Fuentelsaz.—Beispiele interdisziplinärer geowissenschaftlicher Zusammenarbeit* (14–17). Freiburg i. Br.: Informationen Geologisches Landesamt Baden-Württemberg, 8.

Ziegler, P. A. (1990). *Geological atlas of western and central Europe* (2nd ed.). London: Shell Internationale Petroleum Mij. B.V. and Geological Society.